RESEARCH ARTICLE

VIROLOGY

A viral RNA hijacks host machinery using dynamic conformational changes of a tRNA-like structure

Steve L. Bonilla[1], Madeline E. Sherlock[1], Andrea MacFadden[1], Jeffrey S. Kieft[1,2]*

Viruses require multifunctional structured RNAs to hijack their host's biochemistry, but their mechanisms can be obscured by the difficulty of solving conformationally dynamic RNA structures. Using cryo–electron microscopy (cryo-EM), we visualized the structure of the mysterious viral transfer RNA (tRNA)–like structure (TLS) from the brome mosaic virus, which affects replication, translation, and genome encapsidation. Structures in isolation and those bound to tyrosyl-tRNA synthetase (TyrRS) show that this ~55-kilodalton purported tRNA mimic undergoes large conformational rearrangements to bind TyrRS in a form that differs substantially from that of tRNA. Our study reveals how viral RNAs can use a combination of static and dynamic RNA structures to bind host machinery through highly noncanonical interactions, and we highlight the utility of cryo-EM for visualizing small, conformationally dynamic structured RNAs.

RNA's functional versatility derives from its ability to encode genetic information and form complex three-dimensional (3D) structures (*1*). RNA viruses exploit these features, using structured RNA elements to manipulate host machinery and regulate essential viral processes (*2*, *3*). Such RNA elements exist in viral clades as diverse as flaviviruses, lentiviruses, coronaviruses, alphaviruses, and picornaviruses (*2*–*7*), where often a single RNA element performs multiple functions. Our understanding of such RNAs is rudimentary, partly because many are conformationally dynamic and therefore difficult to characterize structurally. Crystallization of such elements is difficult because of their dynamic structure, and nuclear magnetic resonance (NMR) is often not tractable for fully functional RNAs or RNA-protein complexes because of molecular weight limitations (*8*, *9*). Thus, structure-function rules of viral RNAs and their interactions with host machinery are not well understood.

A powerful way that viruses use RNA structure is to mimic cellular tRNAs. Several viral internal ribosome entry sites (IRESs), including that of the hepatitis C virus, mimic parts of tRNA to contact tRNA binding sites on the ribosome (*2*). Additionally, the the HIV-1 RNA genome contains a tRNA-like element that binds lysyl-tRNA synthetase and favors the release of bound $tRNA^{Lys3}$, the primer for HIV reverse transcription (*5*). These and other examples show the importance of tRNA mimicry in diverse viruses, including some that cause human diseases.

[1]Department of Biochemistry and Molecular Genetics, University of Colorado Anschutz Medical Campus, Aurora, CO 80045, USA. [2]RNA BioScience Initiative, University of Colorado Anschutz Medical Campus, Aurora, CO 80045, USA.
*Corresponding author. Email: jeffrey.kieft@cuanschutz.edu

Important examples of tRNA mimicry and multifunctionality are the tRNA-like structures (TLSs) at the 3′ ends of certain positive-strand RNA viral genomes (*10*, *11*). TLSs drive aminoacylation of viral genomic 3′ ends by host aminoacyl-tRNA synthetases (aaRSs) and can interact with other tRNA-specific enzymes, including CCA-nucleotidyltransferase (CCA-NTase) and eukaryotic translation elongation factor 1A (eEF1A) (*10*, *12*). Known TLSs are classified into three types on the basis of their aaRS specificity: valylatable (TLS^{Val}), histidylatable (TLS^{His}), and tyrosylatable (TLS^{Tyr}) (*10*, *12*). Each type has a characteristic secondary structure that differs substantially from that of tRNA, showing that tRNA mimicry can be achieved in diverse ways (fig. S1) (*12*). Of the three types, TLS^{Tyr} differs most from tRNA in size and secondary structure and is the most difficult to reconcile with tRNA mimicry (*13*). The prototype TLS^{Tyr} is found at the 3′ end of each of the three genomic RNAs of the tripartite brome mosaic virus (BMV) genome (Fig. 1A). The BMV TLS^{Tyr} (hereafter referred to as BMV TLS) plays roles in translation, replication, and encapsidation of BMV RNAs; some of these functions are linked to aminoacylation of the TLS, whereas other functions appear to be independent of aminoacylation status (*10*, *13*). The BMV TLS is thus a powerful model system to explore important viral RNA features, including multifunctionality, tRNA mimicry, host protein binding, and potentially conformational dynamics.

Early studies identified the 3′-most 134 nucleotides (nts) of the genomic BMV RNAs as the minimal tyrosylatable TLS RNA (*13*, *14*), but later studies have demonstrated the importance of the adjacent upstream sequence (*13*). The consensus TLS contains 169 nts that form a secondary structure with seven helical stems (compared with four for tRNA), including a pseudoknotted aminoacyl acceptor stem analog (Fig. 1A and fig. S1) (*12*, *15*). Thus, BMV TLS is substantially larger and more structurally complex than tRNA and is therefore an example of a structure that accomplishes tRNA mimicry in a manner that is not readily apparent. It is not known whether BMV TLS contains a tRNA-like L-shaped structure, and conflicting evidence points to either stem B2 or B3 as the anticodon stem analog (Fig. 1A) (*16*). Notwithstanding the lessons that a 3D structure of the BMV TLS could provide about viral RNA structure-function relationships, the structure has remained elusive for decades.

Cryo–electron microscopy (cryo-EM) reveals the global architecture of unbound BMV TLS

We transcribed and purified a TLS sequence from BMV RNA *3* in vitro (*12*, *15*) and confirmed its ability to be tyrosylated in vitro using recombinantly expressed tyrosyl-tRNA synthetase (TyrRS) from model host *Phaseolus vulgaris* (Fig. 1B). Cryo-EM micrographs of this sample collected using a 200-kV microscope contained readily identifiable particles despite their small size (55 kDa) (Fig. 1C and fig. S2). Using a data analysis pipeline that includes the removal of junk particles through 2D classification, ab initio 3D reconstruction, 3D classification, and map refinement (*17*), we obtained an initial 7.0-Å map that displayed characteristics consistent with those of a folded RNA of the expected size (Fig. 1D and fig. S2). The overall architecture of the map was robustly reproduced across ab initio reconstructions with different numbers of classes (fig. S2).

A larger dataset from a 300-kV microscope equipped with an energy filter increased the overall resolution to 4.3 Å. In this map, both minor and major grooves of A-form helices were clearly defined, and the connectivity of the phosphate backbone could be deduced (Fig. 1E and fig. S3). In some regions, stacking and coplanarity of base pairs were resolved, and phosphate bumps were visible (fig. S4). The central core of the map displayed the highest local resolution, but even peripheral-region density was well defined and displayed clear helical features (Fig. 1E).

Notably, one helical domain stood out because it was less defined and had lower local resolution relative to that of other map regions (Fig. 1E, boxed), which suggests local flexibility within the structure. To examine this, we used 3D variability analysis (*18*) to generate a series of 3D volumes representing variability among particles within the dataset (Fig. 1F). This analysis was consistent with this one helical domain occupying multiple conformational states while the rest of the RNA is relatively more static.

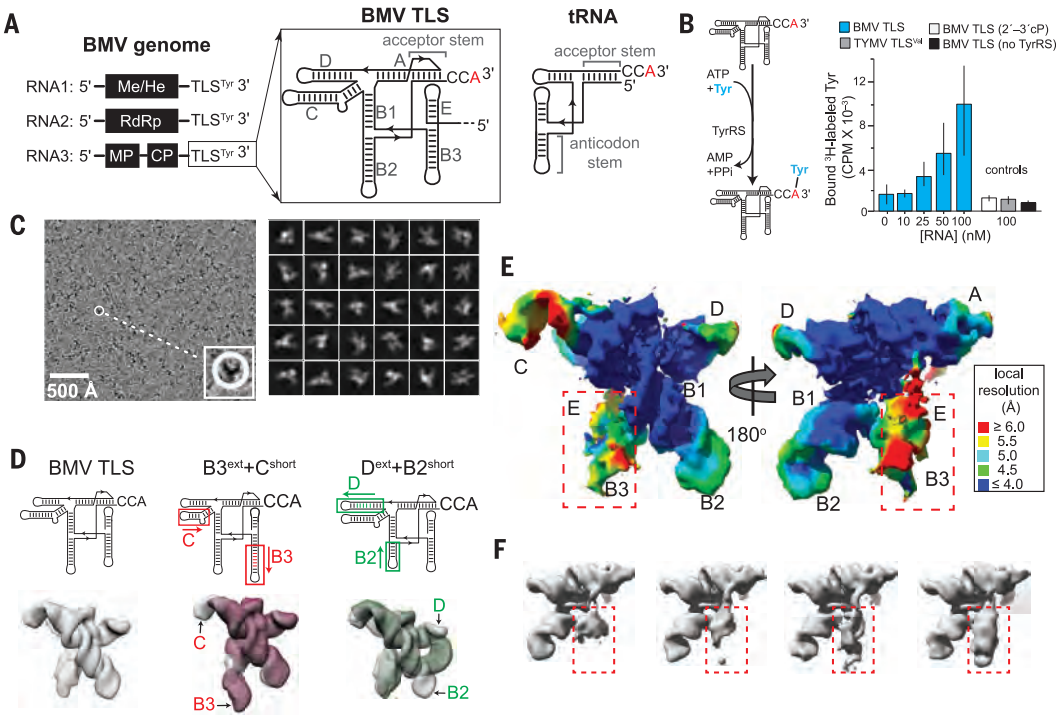

Fig. 1. Functional and initial structural characterization of BMV TLS RNA. (**A**) Organization of the tripartite BMV genome with a TLS at the 3′ end of each RNA. The conserved BMV TLS secondary structure is shown next to that of a tRNA. Structural domains and the terminal CCA are shown, with the red "A" designating the aminoacylation site. Me/He, methyltransferase/helicase; RdRp, RNA-dependent RNA polymerase; MP, movement protein; CP, coat protein. (**B**) (Left) Cartoon of reaction catalyzed by TyrRS. ATP, adenosine 5′-triphosphate; AMP, adenosine 5′-monophosphate. (Right) Tyrosylation of the BMV TLS RNA used for cryo-EM, using an adapted published protocol (*36*). BMV TLS (2′–3′ cP) contains a terminal 2′–3′ cyclic phosphate, not an efficient substrate of TyrRS. TYMV TLS^{Val} is a valylatable TLS from turnip yellow mosaic virus (TYMV). CPM, counts per minute. (**C**) (Left) Representative micrograph of the BMV TLS RNA, 30% of the field of view. Defocus range was −1 to −2.5 μm. (Right) Classified projections from BMV TLS particles (fig. S2). (**D**) Secondary structures and cryo-EM maps of BMV TLS, B3^{ext} + C^{short}, and D^{ext} + B2^{short}. The maps of B3^{ext} + C^{short} (mesh red) and D^{ext} + B2^{short} (mesh green) are superimposed on BMV TLS (solid gray). Arrows point to differences corresponding to altered stems. (**E**) Refined map of BMV TLS at 4.3-Å resolution. Colors denote local resolution. The flexible domain with lower local resolution is boxed in both views. (**F**) Maps representing heterogeneity in the particles using 3D variability analysis (*18*). The variability is mostly localized to the domain that is boxed in red in each map.

Engineered RNAs provide information for unambiguous structural modeling

Aside from low-resolution small-angle x-ray scattering (SAXS) data and a computational model based on chemical probing and functional data (*12*, *19*), there was no prior information on the 3D structure of BMV TLS. To assign RNA helices to regions of the cryo-EM map, we used a strategy based on RNA structural modularity. We designed BMV TLS RNAs with specific helical stems extended or truncated by several base pairs, with the rationale that local differences between the wild-type and modified RNAs would identify the extended and truncated helices within the maps. Analogous experiments have been used to validate structural models or to measure the angles between RNA helices (*20*, *21*).

A map of an RNA with stem B3 extended and stem C shortened displayed local differences compared with that of a wild type that conclusively identified B3 and C (Fig. 1D; B3^{ext} + C^{short}). We repeated this analysis with an RNA with stem D extended and stem B2 shortened (Fig. 1D; D^{ext} + B2^{short}). An unexpected new tertiary interaction apparently formed between the modified helices, but this did not affect the global architecture of the RNA, and local differences between the maps identified stems B2 and D. This strategy, in combination with the previously determined secondary structure (*19*) (Fig. 2A), allowed us to unambiguously identify the positions of all helices with no prior assumptions. This method of obtaining RNA helical assignments in cryo-EM maps is generally applicable and can also validate structural models from automated computational tools (*22*), as discussed below and as has been done previously (*20*).

Cryo-EM yields a complete structural model of BMV TLS

To build a structural model consistent with the cryo-EM data and the secondary structure of BMV TLS, we first evaluated a decades-old computational 3D model (fig. S5) (*19*). The computational model correctly predicted five helical stems emanating from a central core but did not fit well into the experimental map. We built a new structure by docking individual domains into their corresponding density, performing molecular dynamics flexible fitting and real-space refinements, and correcting RNA geometry (Fig. 2B and fig. S6). The entire structure could be built and refined within the map without substantial steric clashes or breaks in the chain (table S1). Models of the extended and truncated constructs (Fig. 1D) support this structural model (fig. S7).

As a complementary method of structural modeling, we used auto-DRRAFTER, a fully automated computational tool that generates multiple unbiased models from a user-provided secondary structure and low-to-moderate–resolution cryo-EM maps (*22*). The models generated by auto-DRRAFTER agreed well with our original structure [root mean square deviation (RMSD) < 3.2 Å] (fig. S6B).

Globally, the BMV TLS structure contains three sets of coaxially stacked extended helical domains (Fig. 2C). One domain comprises helices C, B1, and B2, which form a pseudo-continuous helix that spans the structure, with the apical loops of B2 and C pointing in opposite directions (Fig. 2C, center). The second comprises helices D and A connected through a central four-way junction (4wj) (Fig. 2C, right). Helix A contains the 3′ CCA and serves as both the acceptor stem for tyrosylation and the replication initiation site (*10*). The third corresponds to the conformationally dynamic domain mentioned above (Fig. 1F) and contains helices B3 and E (hereafter referred to as B3 + E) linked to the core of the structure by a single strand of unpaired RNA (Fig. 2C, left). Thus, although atomic-level details are ambiguous at the overall map resolution, the cryo-EM structure of BMV TLS reveals functionally important features.

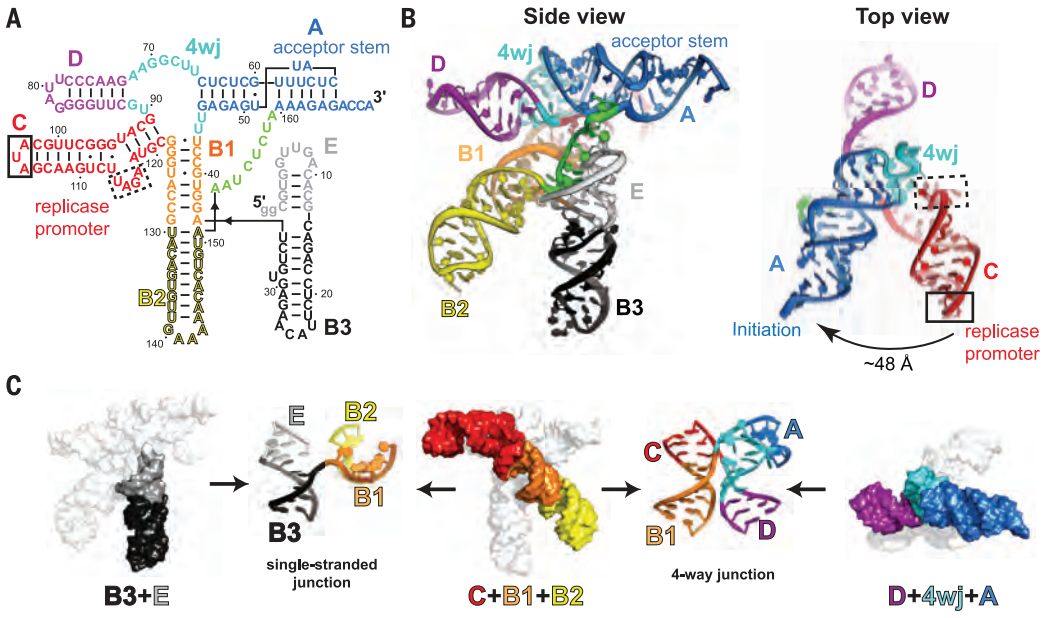

Fig. 2. Structure of free BMV TLS RNA. (**A**) Secondary structure of the BMV TLS RNA construct used for cryo-EM is labeled and colored by domain, with the locations of the replicase promoter and the acceptor stem labeled. The AUA apical triloop (solid box) and UAGA internal loop (dashed box) are critical for replication. (**B**) Structural model of BMV TLS from two views; colors match those in (A). Sequences critical for replication are boxed as in (A). (**C**) The helices, comprising three domains of BMV TLS formed by helical stacks, are highlighted with their corresponding colors: B3 + E (left; black and gray), C + B1 + B2 (middle; red, orange, and yellow), and D + 4wj + A (right; purple, cyan, and blue). The junctions connecting the different domains are shown between them. Colors match those in (A) and (B).

Identification of elements that drive aminoacylation

The ability of the BMV TLS to be aminoacylated has led to the hypothesis that the rules for BMV TLS tyrosylation by TyrRS largely match those of $tRNA^{Tyr}$ (*19*, *23*). Specifically, because $tRNA^{Tyr}$ recognition by the TyrRS requires interactions with its acceptor stem and anticodon loop (with the acceptor stem being more important), analogs of these domains were expected in the BMV TLS structure (*10*, *19*, *24*, *25*). Pseudoknotted helix A was known to be the acceptor stem analog, but the identity of the putative anticodon stem analog was mysterious (*10*, *26*), with conflicting evidence for B3 or B2 (*16*, *19*, *23*, *26*). Our 3D structure shows that although B2 is oriented away from the acceptor stem, the B3 + E domain is positioned such that it is more likely to interact with TyrRS (Fig. 2B). Furthermore, a consensus sequence and secondary structural model based on conservation and covariation analysis of 512 different viral BMV-like TLS^{Tyr} sequences reveals that certain nucleotide identities in B3's apical loop and the length of the B3 + E domain are highly conserved (Fig. 3, A and B). By contrast, stem B2 varies in length with no compensatory changes in the length of B1 (Fig. 3B), and there is no strong conservation in the apical loop of B2 that would suggest it acts as the anticodon (Fig. 3A). The secondary structure model derived from the covariation analysis was validated with chemical probing of three representative TLS^{Tyr} variants (fig. S8). These observations strongly point to B3 as the putative anticodon stem analog.

To further investigate the role of B3, we performed in vitro tyrosylation of BMV TLS variants with terminal loops of B2, B3, or E mutated to UUCG, a loop sequence with a well-determined structure and high thermodynamic stability (*27*). In contrast to previous large sequence deletions (*16*), the UUCG mutations were not expected to affect the overall BMV TLS structure. Electrophoresis of folded BMV TLS mutants under native conditions showed unchanged migration relative to that of the wild type (fig. S9). Although mutations to B3 decreased aminoacylation of the TLS (Fig. 3C), mutations to B2 or E did not have a substantial effect, which suggests that B3 is analogous to the tRNA anticodon. Although the B3 apical loop contains a conserved UACA sequence rather than a canonical tyrosine anticodon (i.e., GUA in plants), the major identity elements of $tRNA^{Tyr}$ lay within its acceptor arm, and the anticodon is less important (*24*); this appears to also be true with BMV TLS.

Free BMV TLS RNA does not contain a classic L-shaped tRNA mimic

To productively interact with TyrRS, it was expected that the BMV TLS acceptor and anticodon stem analogs (stems A and B3, respectively) would comprise a classic tRNA L-shaped fold (Fig. 3D, left). Unexpectedly, stem A and domain B3 + E of BMV TLS are loosely associated, with no interactions analogous to those between the T and D loops in tRNA, and the overall dimensions do not match those of tRNA (Fig. 3D). The implications were apparent when we used the crystal structure of a yeast $tRNA^{Tyr}$-TyrRS complex (*25*) to model BMV TLS bound to TyrRS (Fig. 3E). Superposition of the structure of BMV TLS on $tRNA^{Tyr}$ bound to the TyrRS homodimer, based on their acceptor stems (fig. S10), revealed substantial steric clashes between TyrRS and the B3 + E domain of BMV TLS (Fig. 3E and fig. S10B). This suggests that BMV TLS requires conformational changes to bind TyrRS, and/or binds TyrRS with a geometry that differs from that of canonical tRNA, and/or binds to a different site. The fact that B3 + E is conformationally dynamic made it plausible that interaction with TyrRS requires its rearrangement.

BMV TLS undergoes large conformational changes to bind TyrRS

We applied cryo-EM to the BMV TLS–TyrRS complex (Fig. 4 and figs. S11 and S12). Initial studies with a 200-kV microscope (Fig. 4A) showed two copies of BMV TLS RNA (Fig. 4B, red arrows) bound to opposite sides of the TyrRS homodimer (Fig. 4B, cyan arrow), with each copy making two contacts on the enzyme. This resembles the overall configuration of the $tRNA^{Tyr}$-TyrRS complex (Fig. 4C). However, there is substantially more space between the TLS and the surface of the enzyme compared with $tRNA^{Tyr}$-TyrRS, suggesting different angles between the acceptor and anticodon stems. Consistent with our interpretation of the density, cryo-EM data of free TyrRS (fig. S13) matched the density observed in the center of the BMV TLS–TyrRS complex (Fig. 4B, cyan box).

We collected a larger dataset with a 300-kV microscope at different tilt angles to reduce the effect of preferred particle orientations (fig. S11). Although two bound BMV TLS RNAs are observed in many 2D classes (Fig. 4B and fig. S11), one RNA was consistently better defined in 3D reconstructions, which suggests compositional and/or conformational heterogeneity. Consistent with this, and as

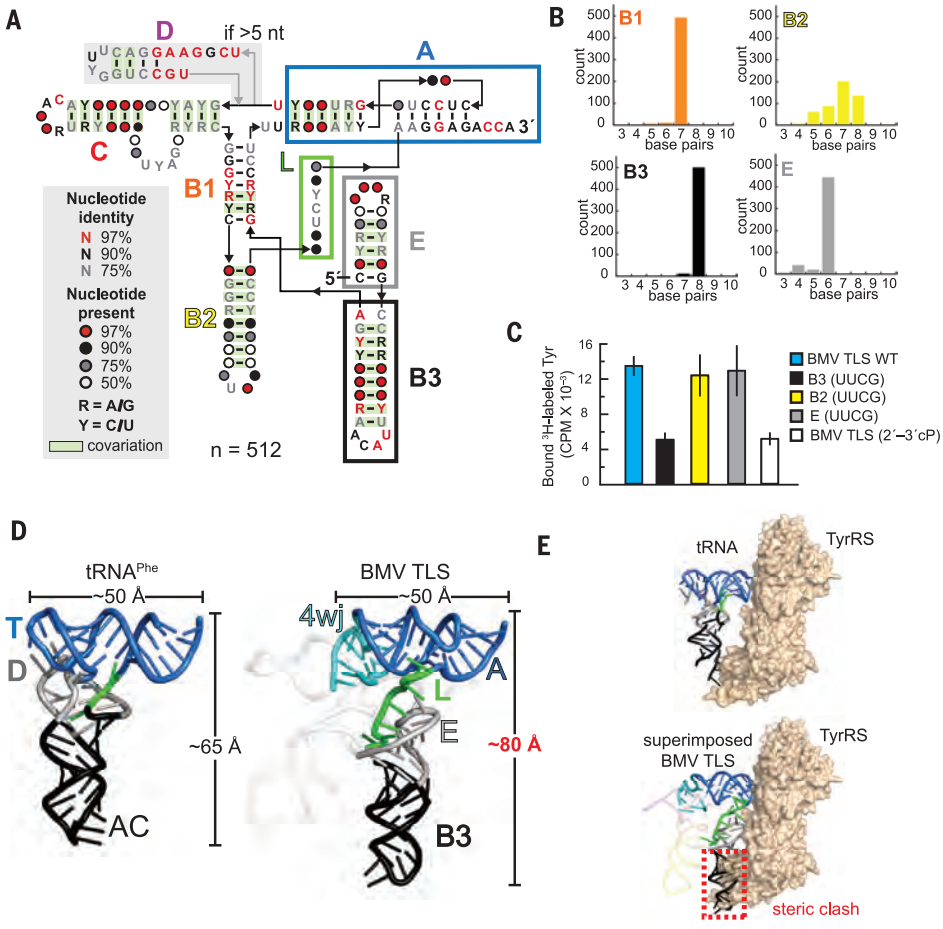

Fig. 3. Structural features of BMV TLS important for replication or tRNA mimicry. (**A**) Consensus covariation and sequence model of TLS^{Tyr} variants related to BMV TLS. Helices are labeled according to BMV TLS. Preliminary alignment of eight TLS^{Tyr} sequences from the Rfam database (*37*, *38*) followed by homology searches resulted in 512 unique sequences used in this consensus model, which is supported by chemical probing of three representative TLS^{Tyr} variants (fig. S9). (**B**) Distribution of lengths of four helices according to the alignment. (**C**) Tyrosylation of mutant BMV TLS. BMV TLS (2′–3′ cP) contains a terminal 2′–3′ cyclic phosphate and thus is not an efficient substrate of TyrRS. (**D**) Comparison of unbound tRNA^{Phe} (left) and tRNA mimicking portions of the BMV TLS (right). The structurally important loops T and D and anticodon (AC) loop are labeled. Analogous structural features are colored as per Fig. 2, and various molecular dimensions are shown. (**E**) (Top) Published crystal structure of yeast tRNA^{Tyr} bound to yeast TyrRS (*25*). (Bottom) The cryo-EM–derived BMV TLS structure overlaid on the bound tRNA^{Tyr} (fig. S11). The steric clash between B3 (anticodon stem analog) and TyrRS is boxed.

discussed below, the data revealed at least two distinct bound conformational states, bound state 1 and bound state 2 (Fig. 4, D and E, and fig. S11). Notably, a previous study had reported that although the TyrRS homodimer has two tRNA^{Tyr} binding sites and crystallizes with two copies of tRNA^{Tyr}, only one tRNA^{Tyr} is aminoacylated at a time (*28*). This apparent paradox may be reflected in the asymmetrical binding behavior of the two BMV TLS RNAs, but further studies are required.

Focusing on a single copy of BMV TLS RNA bound to TyrRS, we obtained interpretable cryo-EM 3D maps of the global conformation of the TLS bound to TyrRS (Fig. 4, D and E, top panels, and fig. S12), with resolutions of 5.5 and 6.0 Å for bound states 1 and 2, respectively (fig. S12). The maps allowed us to fit atomic models of BMV TLS RNA and TyrRS (Fig. 4, D and E, bottom panels).

The structures of the complex show that BMV TLS RNA undergoes a large conformational change to bind TyrRS (Fig. 4F). Specifically, the unbound and bound RNAs were essentially superimposable except for domain B3 + E (fig. S14). In the unbound state, B3 + E occupies a conformational ensemble, mostly positioned at roughly a right angle to the acceptor stem but not properly positioned to interact productively with the enzyme (Fig. 3E). However, in the bound state, B3 + E has rotated ~90° from its average unbound position to lay roughly parallel to the acceptor stem analog (stem A), avoiding any steric clash with the enzyme and placing the B3 apical loop on the surface of TyrRS (Fig. 4, D to F). The bound BMV TLS geometry is very different from that of tRNA^{Tyr}; although BMV TLS also makes two discrete contacts with TyrRS, it has little resemblance to the global L-shaped structure of tRNA^{Tyr}. This bound conformation was not observed in the free RNA, suggesting that it is unstable and rarely adopted without interactions with TyrRS. Thus, the BMV TLS undergoes a marked programmed conformational change to bind the synthetase, in contrast to preorganized tRNAs and TYMV TLS^{Val}—the latter of which nearly perfectly mimics tRNA (*29*).

BMV TLS binds TyrRS in at least two distinct states

The BMV TLS–TyrRS complex adopts two distinct states that may relate to the process of aminoacylation. The overall conformations of the RNA and the enzyme are the same in both states (fig. S14, A and C), but their relative positions differ (Fig. 4, D and E). In bound state 1, the acceptor stem makes limited contacts with TyrRS, and the terminal CCA is well outside the aminoacylation active site (Fig. 4D). In bound state 2, the RNA and the enzyme are closer, the acceptor stem makes deeper contacts with TyrRS, and the terminal CCA is positioned in the active site. Because the position of the acceptor stem in bound state 2 more closely resembles that of tRNA^{Tyr} bound to TyrRS, this state more likely reflects the bound conformation during aminoacylation. However, we cannot make conclusions about the order of events, for example, whether bound state 1 is an on-path intermediate or an alternate nonproductive state. Additionally, because the conformation of the second bound RNA was not resolved, we do not know whether all combinations of bound states 1 and 2 are present or whether there are preferred combinations. Although this behavior may be specific to BMV TLS, it is possible that similar multiple bound states exist in tRNA^{Tyr}-TyrRS complexes, but only a single state was observed by crystallography.

The replicase promoter is prepositioned in proximity to the initiation site

A critical function of BMV TLS is recruiting replication machinery to the initiation site

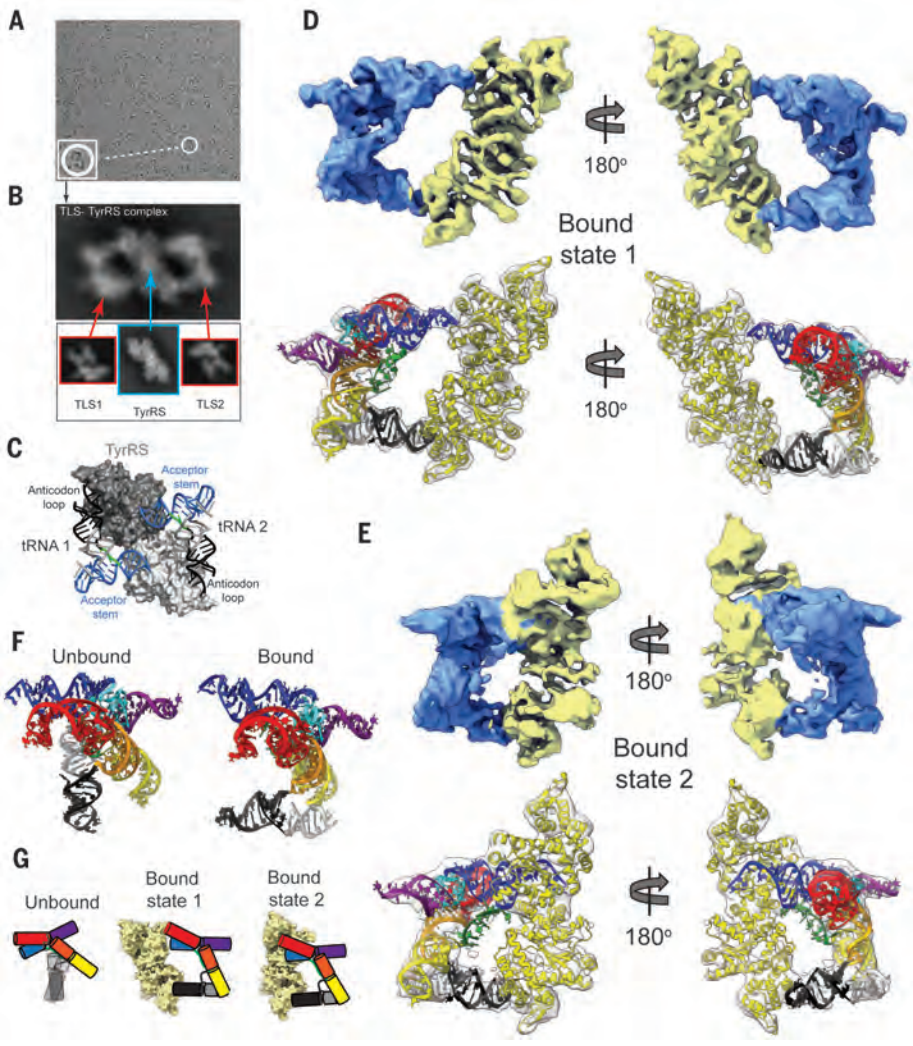

Fig. 4. Cryo-EM of the BMV TLS–TyrRS complex. (**A**) Representative micrograph of the BMV TLS–TyrRS complex with a 200-kV electron microscope. (**B**) Representative 2D class of the complex showing two BMV TLS RNA molecules bound to TyrRS. For comparison, densities of unbound TyrRS (cyan box; fig. S13) and unbound BMV TLS (red boxes; Fig. 1C) are shown. (**C**) Crystal structure of the yeast tRNA-TyrRS complex, with tRNA elements labeled (Protein Data Bank ID: 2dlc). (**D**) A 5.5-Å cryo-EM map of the BMV TLS–TyrRS complex in bound state 1 (top) and an atomic model fitted to the density (bottom). (**E**) A 6.0-Å cryo-EM map of the BMV TLS–TyrRS complex in bound state 2 (top) and an atomic model fitted to the density (bottom). (**F**) Comparison of the structure of BMV TLS in isolation versus when bound to TyrRS. (**G**) Comparison of BMV TLS in an unbound state and two bound states. Colors are as in Fig. 2.

(*13*, *30*, *31*). Although replication initiates at the 3′ end in stem A, the promoter is within stem C's apical AUA triloop (Fig. 2, A and B, solid box) and a UAGA 4-nt bulge (Fig. 2, A and B, dashed box) (*30*–*32*). The structure reveals that helix C is prepositioned adjacent and nearly parallel to helix A (Fig. 2B, right). The resulting distance between the AUA triloop promoter and the replication initiation site is ~48 Å. Because the replication complex consists of multiple viral and host proteins of 43 to 110 kDa (BMV-encoded replication proteins P1 and P2 are 110 and 95 kDa, respectively) (*33*), it is likely large enough to span this distance. Further, the proximity of the UAGA 4-nt bulge (Fig. 2B, dashed box) to the 4wj likely creates tertiary interactions that stabilize the position of stem C relative to helix A (Fig. 2B, right). Overall, the structure suggests that helix C and helix A are prepositioned to reduce the conformational search of the bound replicase for its substrate, but replicase binding, as with TyrRS, could also be associated with additional RNA conformational changes.

Discussion

The BMV TLS has served as a model system for understanding RNA structure-function relationships for decades, but until now its 3D structure had remained elusive. The cryo-EM structures of the BMV TLS in unbound and TyrRS-bound states reveal a strategy for co-opting the cell's machinery using an RNA structure that contains a combination of conformationally dynamic and relatively static elements. The BMV TLS achieves aminoacylation by positioning the CCA at the 3′ end and an anticodon loop analog within an architecture that has little resemblance to that of tRNA, but which spatially arranges them to interact with the TyrRS; the decades-old term tRNA-like structure may be a misnomer for this RNA. This unexpected mode of binding invites speculation that other RNAs with secondary structures that deviate substantially from those of tRNAs may bind aaRSs in noncanonical ways but be difficult to identify on the basis of sequence or secondary structure alone.

The potential function and/or consequences of the conformational change and global fold of BMV TLS are not clear. The conformational change could serve as a signal to initiate synthetase binding or to enable the binding of other proteins to the remodeled structure. In the unbound form, the apical loop of stem E is occluded, but it is exposed in the bound form and in proximity to stem B2; any functional implications of this are unknown. The structure is a combination of preformed and dynamic features. These features might facilitate and organize interactions with the distinct machineries required for replication, recombination, and encapsidation of the viral RNAs (*30*). Other multifunctional RNAs likely utilize similar characteristics to organize different roles.

RNAs exist as conformational ensembles, and dynamics are critical for RNA function (*1*, *8*, *34*). Recent studies have explored cryo-EM as a powerful tool for rapidly solving small RNA-only structures (*22*, *35*), and our studies highlight the potential of cryo-EM for dissecting dynamic processes involving functional structured RNAs and RNA-protein complexes. Unlike crystallographic studies, in which conformational dynamics must largely be inferred or suppressed, cryo-EM offers direct detection of inherent motions. Here, we highlighted a tool that can aid in this task—the use of extensions and/or truncations of modular helical domains in combination with robust secondary structures to rapidly assign specific secondary structural elements to the electron density, provide constraints for structural modeling, and/or validate automated modeling programs. Cryo-EM, in combination with emerging computational tools, will greatly facilitate the study of diverse dynamic regulatory RNAs and RNA-protein complexes.

REFERENCES AND NOTES

1. L. R. Ganser, M. L. Kelly, D. Herschlag, H. M. Al-Hashimi, *Nat. Rev. Mol. Cell Biol.* **20**, 474–489 (2019).
2. Z. A. Jaafar, J. S. Kieft, *Nat. Rev. Microbiol.* **17**, 110–123 (2019).

3. B. M. Akiyama, D. Eiler, J. S. Kieft, *Curr. Opin. Struct. Biol.* **36**, 40–47 (2016).
4. K. Lu *et al.*, *Science* **334**, 242–245 (2011).
5. C. P. Jones, W. A. Cantara, E. D. Olson, K. Musier-Forsyth, *Proc. Natl. Acad. Sci. U.S.A.* **111**, 3395–3400 (2014).
6. D. Yang, J. L. Leibowitz, *Virus Res.* **206**, 120–133 (2015).
7. O. Fernández-Miragall, S. López de Quinto, E. Martínez-Salas, *Virus Res.* **139**, 172–182 (2009).
8. X. Shi, S. Bonilla, D. Herschlag, P. Harbury, *Methods Enzymol.* **558**, 75–97 (2015).
9. K. Murata, M. Wolf, *Biochim. Biophys. Acta Gen. Subj.* **1862**, 324–334 (2018).
10. T. W. Dreher, *WIREs RNA* **1**, 402–414 (2010).
11. R. Giegé, *Proc. Natl. Acad. Sci. U.S.A.* **93**, 12078–12081 (1996).
12. J. A. Hammond, R. P. Rambo, M. E. Filbin, J. S. Kieft, *RNA* **15**, 294–307 (2009).
13. T. W. Dreher, *Virus Res.* **139**, 217–229 (2009).
14. R. L. Joshi, S. Joshi, F. Chapeville, A. L. Haenni, *EMBO J.* **2**, 1123–1127 (1983).
15. M. Vieweger, E. D. Holmstrom, D. J. Nesbitt, *Biophys. J.* **109**, 2625–2636 (2015).
16. P. Fechter, R. Giegé, J. Rudinger-Thirion, *J. Mol. Biol.* **309**, 387–399 (2001).
17. A. Punjani, J. L. Rubinstein, D. J. Fleet, M. A. Brubaker, *Nat. Methods* **14**, 290–296 (2017).
18. A. Punjani, D. J. Fleet, *J. Struct. Biol.* **213**, 107702 (2021).
19. B. Felden, C. Florentz, R. Giegé, E. Westhof, *J. Mol. Biol.* **235**, 508–531 (1994).
20. N. J. Baird *et al.*, *J. Am. Chem. Soc.* **132**, 16352–16353 (2010).
21. T. M. Nakamura, Y. H. Wang, A. J. Zaug, J. D. Griffith, T. R. Cech, *EMBO J.* **14**, 4849–4859 (1995).
22. K. Kappel *et al.*, *Nat. Methods* **17**, 699–707 (2020).
23. V. Perret, C. Florentz, T. Dreher, R. Giege, *Eur. J. Biochem.* **185**, 331–339 (1989).
24. P. Fechter, J. Rudinger-Thirion, A. Théobald-Dietrich, R. Giegé, *Biochemistry* **39**, 1725–1733 (2000).
25. M. Tsunoda *et al.*, *Nucleic Acids Res.* **35**, 4289–4300(2007).
26. T. W. Dreher, T. C. Hall, *J. Mol. Biol.* **201**, 41–55 (1988).
27. M. Molinaro, I. Tinoco Jr., *Nucleic Acids Res.* **23**, 3056–3063 (1995).
28. W. H. Ward, A. R. Fersht, *Biochemistry* **27**, 1041–1049 (1988).
29. T. M. Colussi *et al.*, *Nature* **511**, 366–369 (2014).
30. A. L. Rao, C. Cheng Kao, *Virus Res.* **206**, 46–52 (2015).
31. M. R. Chapman, C. C. Kao, *J. Mol. Biol.* **286**, 709–720 (1999).
32. C.-H. Kim, C. C. Kao, I. Tinoco Jr., *Nat. Struct. Biol.* **7**, 415–423 (2000).
33. R. Quadt, E. M. Jaspars, *Virology* **178**, 189–194 (1990).
34. L. Salmon, S. Yang, H. M. Al-Hashimi, *Annu. Rev. Phys. Chem.* **65**, 293–316 (2014).
35. K. Zhang *et al.*, *Nat. Commun.* **10**, 5511 (2019).
36. E. W. Hartwick *et al.*, *Nat. Commun.* **9**, 5074 (2018).
37. I. Kalvari *et al.*, *Curr. Protoc. Bioinformatics* **62**, e51 (2018).
38. I. Kalvari *et al.*, *Nucleic Acids Res.* **46**, D335–D342 (2018).

ACKNOWLEDGMENTS

E. R. Camacho and P. Van Blerkom (University of Colorado Anschutz Medical Campus, Cryo-EM Facility) and T. Humphreys (Pacific Northwest Center for Cryo-EM) assisted with microscope operation. E. Hartwick helped with the aminoacylation assays. The authors thank current and former Kieft laboratory members for thoughtful discussions and technical assistance as well as A.-L. Steckelberg, B. Akiyama, Q. Vicens, and D. Constantino for critical reading of the manuscript. **Funding:** This work was supported by NIH grants R35GM118070 (J.S.K.) and F32GM139385 (S.L.B.). S.L.B. is a Howard Hughes Medical Institute Hanna Gray Fellow. M.E.S. is a Jane Coffin Childs Postdoctoral Fellow. A portion of this research was supported by NIH grant U24GM129547 and performed at the PNCC at OHSU and accessed through EMSL (grid.436923.9), a DOE Office of Science User Facility sponsored by the Office of Biological and Environmental Research. **Author contributions:** S.L.B. conceptualized the study, performed cryo-EM and aminoacylation experiments, analyzed data, performed structural modeling, and wrote the manuscript in collaboration with J.S.K. M.E.S. performed bioinformatic analysis and chemical probing and edited the manuscript. A.M. purified proteins and edited the manuscript. J.S.K. conceptualized the study, performed structural modeling, acquired funding, and wrote the manuscript in collaboration with S.L.B. **Competing interests:** The authors declare no competing interests. **Data and materials availability:** All data are available in the main text and the supplementary materials. Cryo-EM maps are available in the Electron Microscopy Data Bank with codes EMD-24952, EMD-25023, and EMD-25041. Structural models are available in the Protein Data Bank with codes 7SAM, 7SC6, and 7SCQ.

SUPPLEMENTARY MATERIALS

science.org/doi/10.1126/science.abe8526
Materials and Methods
Figs. S1 to S14
Tables S1 and S2
References (*39*–*60*)
MDAR Reproducibility Checklist
Data S1

View/request a protocol for this paper from *Bio-protocol*.

18 September 2020; resubmitted 27 August 2021
Accepted 4 October 2021
10.1126/science.abe8526

A viral RNA hijacks host machinery using dynamic conformational changes of a tRNA-like structure

Steve L. Bonilla, Madeline E. Sherlock, Andrea MacFadden, and Jeffrey S. Kieft

Science **374** (6570), . DOI: 10.1126/science.abe8526

A tricky mimicry

RNA viruses use dynamic, multifunctional folded elements to hijack host cellular machinery. Bonilla *et al*. used cryo–electron microscopy (cryo-EM) to explore an RNA element from Brome mosaic virus that tricks host cell tyrosine transfer RNA synthetase (TyrRS) into adding a tyrosine to the viral genome's 3# end. Visualizing this RNA both in isolation and bound to a cellular TyrRS revealed a bound structure unlike the canonical transfer RNA L-like shape and conformational rearrangements in the RNA upon binding to the TyrRS, which suggests a multistep process of enzyme recognition. This study highlights the power of cryo-EM to illustrate dynamic processes involving small structured RNAs and RNA-protein complexes. —DJ